

# Self-Assembly of Perovskite for Fabrication of Semitransparent Perovskite Solar Cells

Sigalit Aharon, Michael Layani, Bat-El Cohen, Efrat Shukrun, Shlomo Magdassi, and Lioz Etgar\*

This work reports on the preparation of semitransparent perovskite solar cells. The cells transparency is achieved through a unique wet deposition technique that creates perovskite grids with various dimensions. The perovskite grid is deposited on a mesoporous TiO<sub>2</sub> layer, followed by hole transport material deposition and evaporation of a semitransparent gold film. Control of the transparency of the solar cells is achieved by changing the perovskite solution concentration and the mesh openings. The semitransparent cells demonstrate 20–70% transparency with a power conversion efficiency of 5% at 20% transparency. This is the first demonstration of the possibility to create a controlled perovskite pattern using a direct mesh-assisted assembly deposition method for fabrication of a semitransparent perovskite-based solar cell.

## 1. Introduction

Organic and inorganic materials have been widely used for the development of semitransparent solar cells,<sup>[1–8]</sup> and have been suggested for integration in office buildings and replacement windows. An attractive application of semitransparent photovoltaic (PV) solar cells is the possibility to use them in building integrated elements that can lead to self-sustaining buildings at low cost. This integration offers harvesting of solar energy over wider surfaces.

Perovskite-based solar cells have recently shown impressive PV performance of 20.1% efficiency,<sup>[9]</sup> positioning them as an attractive subject for research.<sup>[10–16]</sup> They combine simple, low-cost deposition methods with high power conversion efficiencies (PCEs), making them promising candidates for low-cost solar-energy harvesting.<sup>[17–19]</sup> So far, there are only a few reports about the development of semitransparent perovskite solar cells. Eperon et al.<sup>[20,21]</sup> used a strategy which relied on the dewetting of the perovskite film to create “perovskite islands,” thus achieving high transmittance but clearly decreasing the overall PCE due to the voids within the active layer. Moreover, it seems that with this method it is difficult to precisely control the transparency of the cell. In recent reports,<sup>[22,23]</sup> a thin perovskite

layer was deposited by evaporation technique. However, evaporation-based processes are very costly, require high capital investments, and are very complicated for upscaling, which is required for industrial applications. Semitransparent top electrode made of silver nanowires was introduced into perovskite-based solar cells.<sup>[24]</sup> The transparency in this case was controlled by the top electrode transparency and not by the perovskite film. In addition, the silver nanowires can be used as an alternative top electrode made by solution-processed technique for semitransparent solar cells.

Here, we report on a unique, simple wet deposition method for the fabrication of semitransparent perovskite-based

solar cells. This deposition method is fundamentally different from previously reported deposition methods of CH<sub>3</sub>NH<sub>3</sub>PbI<sub>3</sub> (MAPbI<sub>3</sub>) perovskite. The film formation in this method is enabled by the mesh-assisted assembly of the perovskite solution through wetting along the wall of a conventional screen printing mesh, as described earlier.<sup>[25–27]</sup> Meaning, here the perovskite is deposited along a controlled pattern through solution-process and in ambient conditions. Semitransparent perovskite solar cells were fabricated; the perovskite grid was deposited upon a mesoporous TiO<sub>2</sub> layer, followed by 2,2',7,7'-tetrakis-(*N,N*-di-4-methoxyphenylamino)-9,9'-spirobifluorene (spiro-OMeTAD) deposition and evaporation of gold back contact. In addition, semitransparent hole conductor free perovskite solar cells (without spiro-OMeTAD as the hole transporting material (HTM)) were prepared for comparison. Nontransparent HTM-free perovskite solar cells were already demonstrated to achieve 10.85% efficiency.<sup>[26–29]</sup> Control of transparency is achieved by changing solution concentrations (wt%) and mesh openings of the printing screen. Using this method, semitransparent cells with 20–70% transparency were fabricated. Ultrahigh resolution scanning electron microscopy (UHR-SEM), optical microscope, and a profilometer were used to characterize the perovskite grids. Intensity-modulated photovoltage spectroscopy (IMVS) was performed for the analysis of the recombination processes occurring in this unique structure of semitransparent perovskite solar cells.

## 2. Results and Discussion

This work describes the preparation of semitransparent perovskite-based solar cells. The perovskite layer of the cell was deposited in ambient environment using simple, low-cost

S. Aharon, M. Layani, B.-E. Cohen, E. Shukrun,  
Prof. S. Magdassi, Dr. L. Etgar  
The Hebrew University of Jerusalem  
Institute of Chemistry  
Casali Center for Applied Chemistry  
Jerusalem 91904, Israel  
E-mail: lioz.etgar@mail.huji.ac.il



DOI: 10.1002/admi.201500118

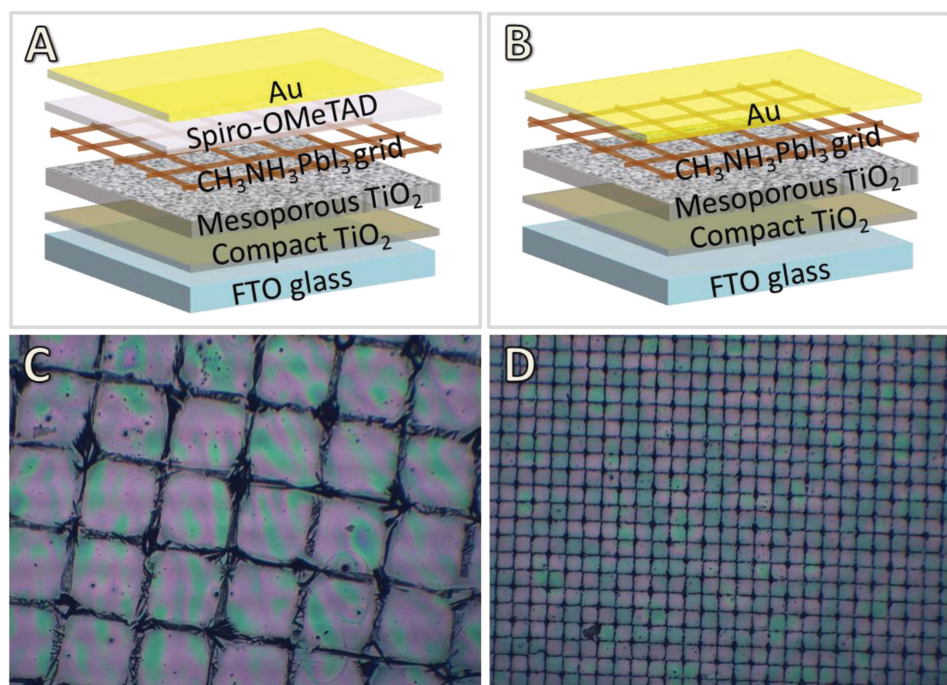


**Figure 1.** A) The structure of the semitransparent cell: FTO glass/TiO<sub>2</sub> compact layer/mesoporous TiO<sub>2</sub>/grid of CH<sub>3</sub>NH<sub>3</sub>PbI<sub>3</sub>/Spiro-OMeTAD/gold. B) The structure of the HTM-free semitransparent cell: FTO glass/TiO<sub>2</sub> compact layer/mesoporous TiO<sub>2</sub>/grid of CH<sub>3</sub>NH<sub>3</sub>PbI<sub>3</sub>/gold. C) Optical microscope image of the wide grid: opening of ≈200 μm. D) Optical microscope image of the dense grid: opening of ≈60 μm.

mesh-assisted assembly deposition method (followed by annealing process). The transparency measurements and photovoltaic characterizations showed strong correlation between the photovoltaic activity of the cell and its average transparency between 400 and 800 nm. When changing the parameters of the perovskite deposition process (mesh opening and solution concentration), the transparency was changed and the photovoltaic activity of the cells varied accordingly.

The structure of the perovskite-based solar cells is as follows: FTO glass/TiO<sub>2</sub> compact layer/mesoporous TiO<sub>2</sub>/grid of Perovskite/spiro-OMeTAD/thin film of gold (Figure 1A). In the case of the HTM-free semitransparent perovskite solar cells, the structure was identical, excluding the spiro-OMeTAD layer (Figure 1B). Due to the controlled voids in the perovskite grid, which enable the transparency of the solar cell, a direct contact is formed between the HTM and the mesoporous TiO<sub>2</sub> film (or between the gold back contact and the mesoporous TiO<sub>2</sub> film, in the case of HTM-free solar cells). Interestingly, despite those voids, the semitransparent devices with and without HTM showed power conversion efficiency of 4.98% and 2.55% respectively for 19% transparency. The perovskite grid was obtained through wetting of the perovskite precursor solution along the walls of a screen printing mesh which was placed on the mesoporous TiO<sub>2</sub> layer. As shown below, the transparency of the cell can be simply controlled by two parameters, (i) mesh opening and (ii) the precursor solution concentration.

Following the deposition of the compact and mesoporous TiO<sub>2</sub> layers, a solution of PbI<sub>2</sub> and MAI in DMF was placed on top of the screen printing mesh. Due to the presence of the wetting agent, the solution immediately wets the surface and fills the gap between the screen printing mesh and the mesoporous

TiO<sub>2</sub> layer. During solvent evaporation, the PbI<sub>2</sub> and MAI molecules aligned along the mesh wires due to capillary forces. The screen printing mesh was removed after the DMF evaporation was completed, and a grid pattern was obtained, in which the walls contain crystalline perovskite formed in situ from PbI<sub>2</sub> and MAI. An additional annealing step is necessary to complete the crystallization.

Figure 1C,D presents optical-microscope images of two different CH<sub>3</sub>NH<sub>3</sub>PbI<sub>3</sub> perovskite grids fabricated on top the mesoporous TiO<sub>2</sub> surface, by using meshes with different openings: wide opening (Figure 1C, grid opening of ≈200 μm), and narrow opening (Figure 1D, grid opening of ≈60 μm). In general, it was found that the grid opening size can be easily controlled by the mesh opening size, thus enabling control of the transparency of the perovskite film (which is actually empty squares surrounded by perovskite crystals). The PCE is affected by the grid opening, i.e., when the grid opening is large, the PCE is decreased since the active area is smaller and there are more contact points between the HTM and the mesoporous TiO<sub>2</sub>. Moreover, no perovskite crystals are present at the open areas in the perovskite grid as shown in Figures 1C,D and 2A (see also Figure S1 in the Supporting Information). The absence of perovskite crystals in the voids supports the efficient control over the final assembly of the perovskite attained by using this deposition method.

Figure 2A depicts UHR-SEM image of the perovskite grid on top of the mesoporous TiO<sub>2</sub> layer. It can be seen that the perovskite crystals formed a super-structure of thin needle-like assemblies (see also Figure S2 in the Supporting Information), which were present only where the original mesh lines were located.

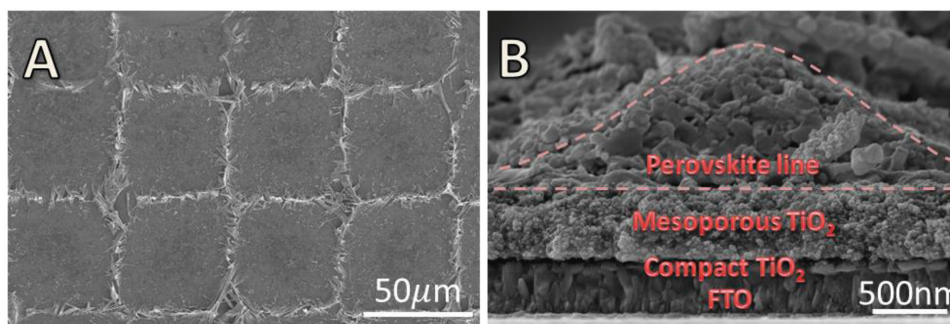


**Figure 2.** A) UHR-SEM image of perovskite dense grid (top view). B) UHR-SEM cross-section image of the HTM-free cell where the grid line of  $\text{CH}_3\text{NH}_3\text{PbI}_3$  perovskite can be observed. The mesh opening was  $\approx 60 \mu\text{m}$  and the assembly solution concentration is 12.5 wt% (about 40% transparency).

Figure 2B presents a cross-section UHR-SEM image of an HTM-free semitransparent solar cell. The perovskite line of the grid can be observed on top of the mesoporous  $\text{TiO}_2$  layer (the grid boundaries are marked in the Figure). The height and the width of the perovskite grid can be controlled by changing the concentration of the  $\text{PbI}_2$  and MAI in the precursor solution, as shown in Figure 3 for mesh with openings of  $\approx 60 \mu\text{m}$ .

As seen in Figure 3A, the average height (relative to the  $\text{TiO}_2$  layer) of the grid line increases while increasing the solution concentration. However, the width has the same values when using concentrations between 7.5 and 15 wt%, and starts to increase only above this concentration. There is a minimal line width which is a result of the capillary forces between the perovskite molecules and the mesoporous  $\text{TiO}_2$  layer, meaning, even at low concentrations this width is expected to be covered by molecules. Figure 3B shows the average area of the grid line cross-section, (calculated by multiplying the average width of a specific grid line with the average height of the same grid line). As expected, the area of the grid line cross-section is increased while increasing the concentration of the components of the perovskite precursor solution.

The photovoltaic performance of various assembly solution concentrations using dense grids with opening of  $\approx 60 \mu\text{m}$  are presented in Table 1 (see also Table S1 in the Supporting Information for the photovoltaic activity of the HTM-free semitransparent perovskite-based solar cells). The PCE of the cells decreases with the increase in transparency (Figure 4A),

which is controlled by the precursor solution concentration (Figure 4B). This is expected since the grid lines which are formed by the low concentration solution have smaller average widths and heights (Figure 3A) than those of the grid lines formed from a more concentrated assembly solution. Moreover, Figure 4A,B shows the reproducibility of the different cells using various concentrations. The efficiencies and the transparencies are more widely distributed when increasing the solution concentration.

Figure 4C shows the images of the cells with different transparencies (which were controlled by changing the assembly concentration solution from 7.5 to 20 wt%, from right to left). The current–voltage curves of the semitransparent perovskite solar cells are presented in Figure 4D for different cell transparencies.

The transparency control by the perovskite grid formation has an important advantage, which is the possibility to calculate the exact coverage of the perovskite grid in the active area (see detailed calculation in the Supporting Information). Using this unique mesh-assisted assembly deposition method, it is possible to accurately design the required coverage and transparency of the solar cell. The coverage of the cell is the fraction of area that is covered by the perovskite grid lines, without the grid voids (in which there is no perovskite). It was observed that the coverage of the perovskite solar cells prepared using assembly solution concentrations of 7.5, 10, 12.5, and 15 wt% are similar ( $\approx 35\% \pm 3\%$  of the

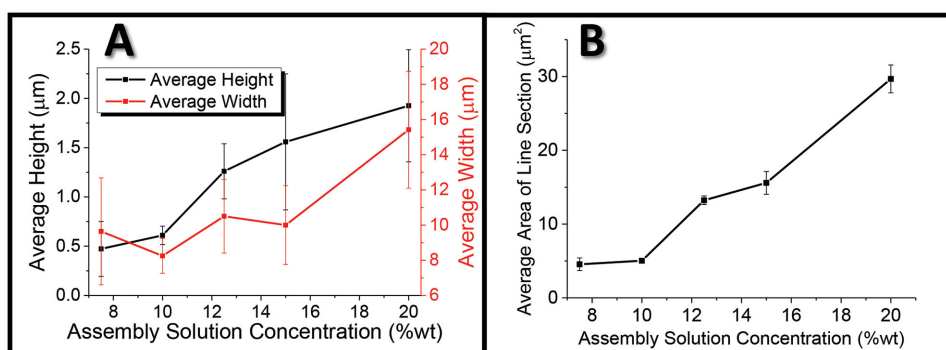


**Figure 3.** The grid dimensions versus the assembly solution concentration (measured by profiler). A) The average height and width ( $\mu\text{m}$ ; full width at half maximum, FWHM) of the grid lines resulted from the use of different concentrations of the assembly solutions (wt%). B) The average cross-section area of a grid line (calculated by multiplying the average width line with the average height of the same grid line) versus assembly solution concentration.

**Table 1.** PV parameters, average transparency (%) between 400 and 800 nm, and coverage (%) of the various semitransparent cells.

Assembly solution concentration [%]	Transparency [%]	$V_{oc}$ [V]	$J_{sc}$ [ $\text{mA cm}^{-2}$ ]	FF [%]	Efficiency [%]	Coverage [%]
20	19	0.68	14.87	49	4.98	53
15	25	0.71	10.50	51	3.79	31
12.5	38	0.53	4.32	45	1.04	38
10	46	0.49	3.14	53	0.83	37
7.5	67	0.61	1.31	48	0.38	35

area is covered by the perovskite grid lines), while only the coverage of cells that were prepared using assembly solution concentration of 20 wt%, the coverage was different ( $\approx 50\%$ ). The increase in the coverage for the 20 wt% solution concentration can be expected already from the profile measurements (Figure 3A) in which the width of the grid lines was about the same average values in the case of the lower concentrations (till 15 wt%). However, despite the fact that the coverage of the cells in the case of the lower assembly solution concentrations was similar, the cells' PV performance was different as shown in Table 1. The reason for the difference in PV performance might be due to the fact that the coverage calculations do not

take into account the thickness of the perovskite lines, which dramatically affects the PV performance.

An interesting outcome is related to the unique structure of the semitransparent perovskite solar cells presented in this work. In this solar cell structure, there is an intrinsic direct contact between the HTM and the mesoporous  $\text{TiO}_2$  film (or between the gold back contact and the mesoporous  $\text{TiO}_2$  film, in the case of HTM-free perovskite cells), which means large recombination centers. Even though, a reasonable PV performance was achieved. For example, in the case of 50% coverage,  $J_{sc}$  of  $14.87 \text{ mA cm}^{-2}$  with  $V_{oc}$  of 0.68 V were achieved. The reasonable PV performance can be attributed to the long diffusion length<sup>[13]</sup> and high absorption coefficient<sup>[30]</sup> of the  $\text{MAPbI}_3$  perovskite. Moreover, in the absence of HTM  $J_{sc}$  of  $9 \text{ mA cm}^{-2}$  with  $V_{oc}$  of 0.63 V were achieved. This further supports our previous reports on the possibility to avoid the need for HTM in the perovskite solar cells and demonstrates the superior properties of the perovskite.<sup>[26–28]</sup>

In the case of semitransparent solar cells which include HTM layer, the recombination centers are mainly at the interface spiro-OMeTAD/mesoporous  $\text{TiO}_2$  (see Figure 1A), while in the semitransparent HTM-free cells, the main recombination may occur at the interface mesoporous  $\text{TiO}_2/\text{Au}$  (see Figure 1B). IMVS measurement were performed on both semitransparent HTM cells and semitransparent HTM-free cells in order to

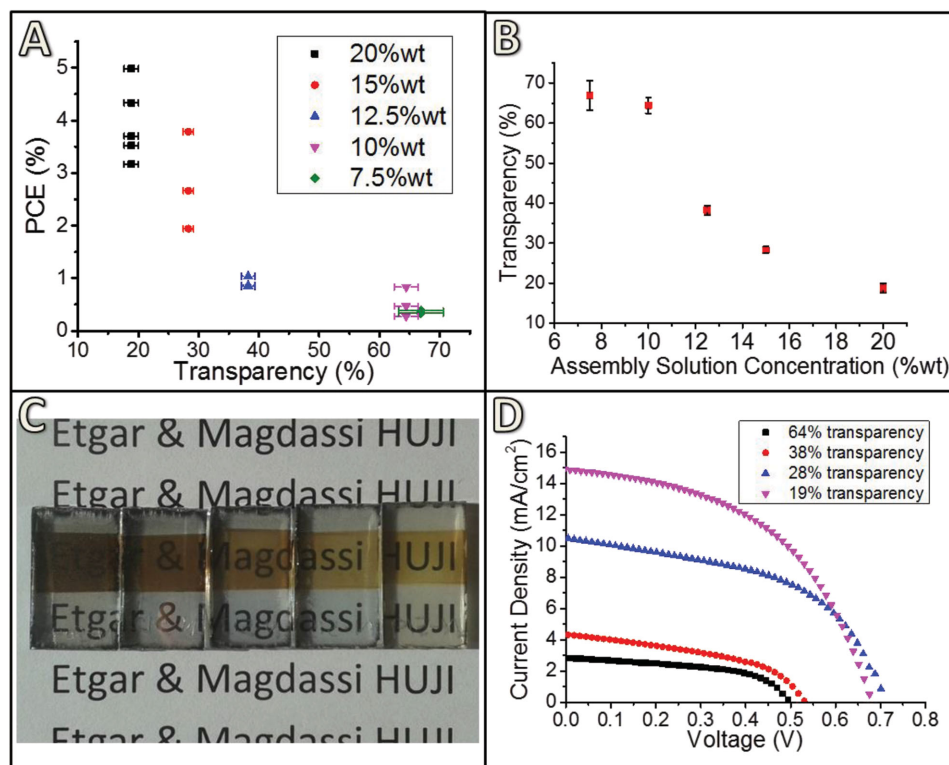


**Figure 4.** A) The PCE of the semitransparent cells versus their average transparency calculated in the range of 400–800 nm wavelengths (the different colors represent the different solution concentrations). B) The average transparency of the perovskite solar cells versus the concentration (wt%) of the assembly solution of the precursors. C) Images of the semitransparent cells with different average transparencies from left to right, 19%, 28%, 38%, 64%, and 67%. D) The current–voltage curves of the semitransparent cells with different average transparencies. The PCEs of the cells are 0.83%, 1.04%, 3.79%, and 4.98% for the cells of 64%, 38%, 28%, and 19% transparency, respectively.

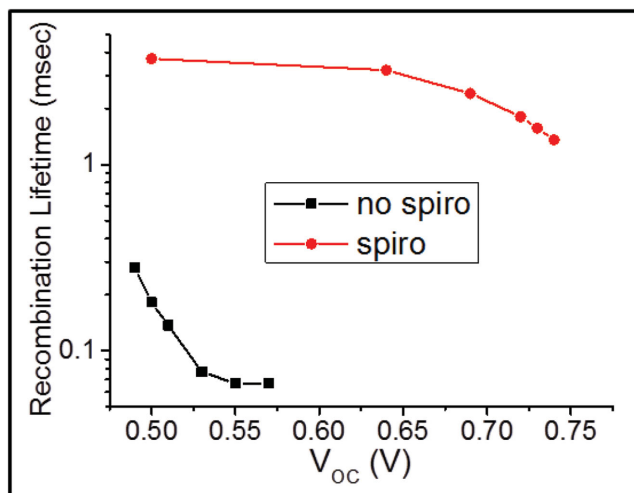


**Figure 5.** The recombination lifetimes which were extracted from the IMVS measurement for the cells with and without HTM versus  $V_{OC}$ .

extract the recombination lifetime<sup>[31–33]</sup> at these solar cells. **Figure 5** shows the recombination lifetime of representative semitransparent perovskite solar cells with and without HTM.

It can be observed that in the case of using HTM in these semitransparent perovskite solar cells the recombination lifetime increases dramatically compared to cells without HTM. The charges are longer lived when HTM was introduced into the device structure.

This supports the higher open-circuit voltages observed for the cells with HTM compared to the HTM-free cells. Moreover, in the case of the HTM-based cells it can be seen that even though a direct contact occurs between the HTM and the mesoporous  $TiO_2$  film, this main recombination channel has almost constant recombination lifetime (Figure 5) with a slight decrease with the increase of the voltage. This can suggest that these unique semitransparent perovskite solar cells have good photovoltaic stability for a wide range of light intensities.

### 3. Conclusions

Semitransparent perovskite-based solar cells were fabricated using simple deposition methods. The transparency of the cells was controlled by changing the opening of the mesh used for the perovskite grid assembly and by varying the concentrations of the perovskite precursor solutions. Optical microscopy, UHR-SEM and profilometry confirmed that the perovskite layer is well confined within the grid lines. So far, the best PV performance for the semitransparent solar cells showed PCE of 4.98% with transparency of 19% (achieved by controlling the transparency), which is comparable to recent report on semitransparent perovskite-based solar cell.<sup>[20]</sup> Further improvement can be achieved by better control of additional parameters of the grid formation, such as the solvent evaporation rate, and the wetting agent type and concentration, which could result in fewer defects in the perovskite grid.

### 4. Experimental Section

**Precursor Synthesis:** Methyl ammonium iodide (MAI) was synthesized by reacting 27.8 mL of methylamine (40% in methanol, TCI) with 30 mL of hydroiodic acid (57 wt% in water, Aldrich) in a 250 mL round bottom flask at 0 °C for 2 h while stirring. The precipitate was recovered by removal of the solvent by a rotary evaporator at 50 °C for 1 h. The white product was washed with ethanol by stirring the mixture for 30 min. Then the mixture was filtered and washed with diethylether. The washing step was repeated three times. After filtration, the solid was collected and dried at 60 °C in a vacuum oven for 24 h.

**Device Fabrication:** The substrate of the device was a  $SnO_2:F$  (FTO) conducting glass ( $15 \Omega \text{ cm}^{-1}$ , Pilkington). A blocking layer was deposited on the FTO glass using a solution of titanium diisopropoxidebis(acetyl acetonate) (TiDIP, 75% in isopropanol, Aldrich) in ethanol. The TiDIP solution was spin coated and then annealed at 450 °C for 30 min. The  $TiO_2$  paste (Dyesol, DSL-90T) was diluted in ethanol (dilution of 0.1 g of the paste in 0.32 g of ethanol absolute), then spin coated on top of the compact  $TiO_2$  layer and annealed at 500 °C for 30 min subsequent to  $TiCl_4$  treatment for 30 min at 70 °C and annealing at 500 °C for 30 min. For the perovskite layer,  $PbI_2$  and MAI were dissolved in DMF in the following concentrations: 7.5, 10, 12.5, 15, and 20 wt%. The fabrication of the semitransparent perovskite grid was conducted directly on the  $TiO_2$  layer. The process of fabrication of a transparent grid was reported elsewhere in the context of preparing transparent conductive coatings.<sup>[34,35]</sup> In this research, a screen printing stainless steel mesh (Ponger 2000 Israel) was placed onto the mesoporous  $TiO_2$  layer which is placed in a closed box with a humidity of 30%–40% RH, and  $\approx 20$  °C. Prior to the placement, the mesh was hydrophilized by plasma cleaning (in 20% oxygen for 2 min, PICO System, Deiner Electronics) in order to enable wetting and movement of the liquid toward the wires of the mesh. Next, 7  $\mu\text{L}$  droplet of the perovskite precursor solution ( $PbI_2$  and MAI in DMF with 0.5 wt% of Byk 333 wetting agent (Byk, Germany)) was placed on top of the mesh. Upon contact, the liquid immediately wets the mesh walls and filled the gap between the mesh and the  $TiO_2$  layer. During evaporation of the DMF, the perovskite precursor solution self-assembled along the walls of the mesh. This is caused due to coffee stain effect which pulls the liquid outwards, and due to capillary forces between the wires of the mesh and the substrate ( $TiO_2$  layer) which induce the alignment of the perovskite precursor molecules along the wires of the mesh. After 20 min, the mesh was removed, leaving a grid pattern composed of the perovskite precursors on the  $TiO_2$  layer. Two types of meshes were used (Figure 1C,D): stainless steel and polyester mesh (Ponger 2000, Israel). The diameters of the two types of mesh wires were (i) 16  $\mu\text{m}$  with 60  $\mu\text{m}$  spacing between the wires and (ii) 25  $\mu\text{m}$  with 200  $\mu\text{m}$  spacing between the wires. Following the mesh-assisted assembly step, the samples were annealed at 90 °C for 30 min. During annealing, a grid composed of  $MAPbI_3$  was formed, as indicated by the dark brown color of the electrodes. The spiro-OMeTAD HTM was deposited by spin coating 40  $\mu\text{L}$  of the following described solution (4000 rpm, 30 s). The solution was prepared by dissolving 72.3 mg of 2,2',7,7'-tetrakis-(*N,N*-di-4-methoxyphenylamino)-9,9'-spirobifluorene (spiro-OMeTAD) in 1 mL chlorobenzene. 26.3  $\mu\text{L}$  of bis(trifluoromethane)sulfonimide lithium salt in acetonitrile (520 mg  $\text{mL}^{-1}$ ), 29  $\mu\text{L}$  of tris(2-(<sup>1</sup>H-pyrazol-1-yl)-4-*tert*-butylpyridine)-cobalt(III) tri s(bis(trifluoromethylsulfonyl)imide)) in acetonitrile (300 mg  $\text{mL}^{-1}$ ) and 19.2  $\mu\text{L}$  of 4-*tert*-butylpyridine were added to the spiro-OMeTAD solution as additives. Finally, the back contact was deposited by evaporating 40 nm of gold under pressure of  $5 \times 10^{-6}$  Torr. The active area was 0.09  $\text{cm}^2$ .

**PV Characterization:** PV measurements were made on a New Port System, composed of an Oriel  $I$ - $V$  test station using an Oriel Sol3A simulator. The solar simulator was class AAA for spectral performance, uniformity of irradiance, and temporal stability. The solar simulator was equipped with a 450 W xenon lamp. The output power was adjusted to match AM1.5 global sunlight ( $100 \text{ mW cm}^{-2}$ ). The spectral match classifications were IEC60904–9 2007, JIC C 8912, and ASTM E927–05.  $I$ - $V$  curves were obtained by applying an external bias to the cell and measuring the generated photocurrent with a Keithley Model 2400 digital

source meter. The voltage step and delay time of the photocurrent were 10 mV and 40 ms, respectively.

**Transmittance Measurements:** UV-vis transmittance spectra were performed using a Jasco V-670 spectrophotometer. The measured transparency is the transparency of the whole cell except the spiro-OMeTAD and the gold contact. The average transparency was calculated between 400 and 800 nm wavelengths.

**Morphology Evaluation:** The grids were observed by optical microscope (MRC Israel), and by a Veeco Dektak 150 profilometer.

**Ultrahigh Resolution Scanning Electron Microscopy (UHR-SEM):** It was performed by Sirion UHR SEM (FEI, Field Emission Instruments), The Netherlands. The measurement conditions were 5 kV at various magnifications.

**Intensity Modulated Photovoltage Spectroscopy (IMVS):** The photocarrier recombination times at open circuit were measured by IMVS. The IMVS measurements were performed using Autolab FRA32M LED driver equipped with a white light source, illuminating from the substrate side. The photovoltaic cells were illuminated with a bias light intensity with a sinusoidal wave modulation. The amplitude of the modulated photovoltage density was kept at 10% or lower compared to the steady-state photovoltage density, with frequencies ranging from 1 Hz to 20 kHz.

## Supporting Information

Supporting Information is available from the Wiley Online Library or from the author.

## Acknowledgements

The authors would like to thank the financial support of Israel Alternative Energy Foundation (I-SAEF), the Ministry of Industry Trade and Labor Office of the Chief Scientist Kamin Project No. 50303, the Tashtiot project of the Office of the Chief Scientist, the FTA program of Israel National Nanotechnology Initiative, the Israel Ministry of Science, the Israel Ministry of Science and Space, and the Campus for Research Excellence and Technological Enterprise (CREATE), which is supported by the National Research Foundation, Prime Minister's Office, Singapore, and Space, and the Campus for Research Excellence and Technological Enterprise (CREATE), which is supported by the National Research Foundation, Prime Minister's Office, Singapore, for their support of applied research project.

Received: March 3, 2015

Revised: May 1, 2015

Published online: June 8, 2015

- [1] J. W. Lim, S. H. Lee, D. J. Lee, Y. J. Lee, S. J. Yun, *Thin Solid Films* **2013**, *547*, 212.  
 [2] Y. T. Chae, J. Kim, H. Park, B. Shin, *Appl. Energy* **2014**, *129*, 217.  
 [3] H. W. Lin, Y. H. Chen, Z. Y. Huang, C. W. Chen, L. Y. Lin, F. Lin, K. T. Wong, *Org. Electron.* **2012**, *13*, 1722.  
 [4] M. Reinhard, R. Eckstein, A. Slobodsky, U. Lemmer, A. Colmann, *Org. Electron.* **2013**, *14*, 273.

- [5] J. Mescher, S. W. Kettlitz, N. Christ, M. F. G. Klein, A. Puetz, A. Mertens, A. Colmann, U. Lemmer, *Org. Electron.* **2014**, *15*, 1476.  
 [6] J. Czolk, A. Puetz, D. Kutsarov, M. Reinhard, U. Lemmer, A. Colmann, *Adv. Energy Mater.* **2013**, *3*, 386.  
 [7] N. G. Park, K. Kim, *Phys. Status Solidi. (A)* **2008**, *205*, 1895.  
 [8] A. K. Pandey, I. D. W. Samuel, *IEEE J. Sel. Top. Quantum Electron.* **2010**, *16*, 1560.  
 [9] [http://www.nrel.gov/ncpv/images/efficiency\\_chart.jpg](http://www.nrel.gov/ncpv/images/efficiency_chart.jpg). Accessed: March 2015.  
 [10] A. Kojima, K. Teshima, Y. Shirai, T. Miyasaka, *J. Am. Chem. Soc.* **2009**, *131*, 6050.  
 [11] O. Malinkiewicz, A. Yella, Y. H. Lee, G. M. Espallargas, M. Graetzel, M. K. Nazeeruddin, H. J. Bolink, *Nat. Photonics* **2014**, *8*, 128.  
 [12] D. Liu, T. L. Kelly, *Nat. Photonics* **2014**, *8*, 133.  
 [13] S. D. Stranks, G. E. Eperon, G. Grancini, C. Menelaou, M. J. P. Alcocer, T. Leijtens, L. M. Herz, A. Petrozza, H. J. Snaith, *Science* **2013**, *342*, 341.  
 [14] J. You, Z. Hong, Y. M. Yang, Q. Chen, M. Cai, T. B. Song, C. C. Chen, S. Lu, Y. Liu, H. Zhou, Y. Yang, *ACS Nano* **2014**, *8*, 1674.  
 [15] M. Graetzel, *Nat. Mater.* **2014**, *13*, 838.  
 [16] M. He, D. Zheng, M. Wang, C. Lin, Z. Lin, *J. Mater. Chem. A* **2014**, *2*, 5994.  
 [17] D. Bi, S. J. Moon, L. Huggman, G. Boschloo, L. Yang, E. M. J. Johansson, M. K. Nazeeruddin, M. Graetzel, A. Hagfeldt, *RSC Adv.* **2013**, *3*, 18762.  
 [18] Y. Liu, H. Zhou, Z. Hong, S. Luo, H. S. Duan, H. H. Wang, Y. Liu, G. Li, Y. Yang, *J. Am. Chem. Soc.* **2014**, *136*, 622.  
 [19] G. E. Eperon, V. M. Burlakov, B. Docampo, A. Goriely, H. J. Snaith, *Adv. Funct. Mater.* **2014**, *24*, 151.  
 [20] G. E. Eperon, V. M. Burlakov, A. Goriely, H. J. Snaith, *ACS Nano* **2014**, *8*, 591.  
 [21] G. E. Eperon, D. Bryant, J. Troughton, S. D. Stranks, M. B. Johnston, T. Watson, D. A. Worsley, H. J. Snaith, *J. Phys. Chem. Lett.* **2015**, *6*, 129.  
 [22] C. Roldan, O. Malinkiewicz, R. Betancur, G. Longo, C. Momblona, F. Jaramillo, L. Camacho, H. J. Bolink, *Energy Environ. Sci.* **2014**, *7*, 2968.  
 [23] L. K. Ono, S. Wang, Y. Kato, S. R. Rega, Y. Qi, *Energy Environ. Sci.* **2014**, *7*, 3989.  
 [24] F. Guo, H. Azimi, Y. Hou, T. Przybilla, M. Hu, C. Bronnbauer, S. Langner, E. Spiecker, K. Forbericha, C. J. Brabec, *Nanoscale* **2015**, *7*, 1642.  
 [25] K. Higashitani, C. E. McNamee, M. Nakayama, *Langmuir* **2011**, *27*, 2080.  
 [26] S. Aharon, B. E. Cohen, L. Etgar, *J. Phys. Chem. C* **2014**, *118*, 17160.  
 [27] B. E. Cohen, S. Gamliel, L. Etgar, *APL Materials* **2014**, *2*, 081502.  
 [28] W. Abu-Laban, L. Etgar, *Chem. Lett.* **2012**, *41*, 397.  
 [29] J. Shi, J. Dong, S. Lv, Y. Xu, L. Zhu, J. Xiao, X. Xu, H. Wu, D. Li, Q. Meng, *Appl. Phys. Lett.* **2014**, *104*, 063901.  
 [30] A. Kojima, M. Ikegami, K. Teshima, T. Miyasaka, *Chem. Lett.* **2012**, *41*, 397.  
 [31] E. Guillen, F. J. Ramos, J. A. Anta, S. Ahmad, *J. Phys. Chem. C* **2014**, *118*, 22913.  
 [32] Y. Zaoh, A. M. Nardes, K. Zhu, *J. Phys. Chem. Lett.* **2014**, *5*, 490.  
 [33] Y. Zaoh, K. Zhu, *J. Phys. Chem. Lett.* **2013**, *4*, 2880.  
 [34] M. Layani, S. Magdassi, *J. Mater. Chem.* **2011**, *21*, 15378.  
 [35] M. Layani, P. Darmawan, W. L. Foo, L. Liu, A. Kamyshny, D. Mandler, S. Magdassi, P. S. Lee, *Nanoscale* **2014**, *6*, 4572.